Chapter 2
Analysis of the Current Ripple in Three-Phase Two-Level VSIs

2.1 Introduction

Three-phase voltage source inverters (VSIs) are widely utilized in ac motor drives, controlled rectifiers, and in general grid-connected applications as dc–ac power conversion devices. The topology of the three-phase inverter with a generic three-phase *R–L–EMF* load (RLE) is given in Fig. 2.1. Most of VSI applications employ carrier-based PWM (CB-PWM) control schemes due to their simplicity of implementation, both in analog and digital ways, fixed switching frequency and well defined harmonic spectrum characteristics [1]. Furthermore, switching losses are easier to control with constant switching frequency, and the inverter design can take advantage of an accurate losses calculation. Different types of CB-PWM together with space vector PWM (SV-PWM) are investigated, and optimal solutions are proposed with reference to reduce the current ripple and switching losses [2–4]. CB-PWM leads to equivalent switching patterns as SV-PWM by proper zero-sequence modulating signal injection [5].

A complete analysis of three-phase PWM converter system addressed to switching losses, dc link harmonics, and inverter input/output harmonics is given by [6]. It has been shown that reduction of the output current harmonics in case of continuous PWM can be achieved by proper zero-sequence signal injection. A further reduction of the RMS value of the current ripple is possible in some cases by development of discontinuous PWM schemes, which allow increasing the carrier frequency while maintaining the switching losses as same as continuous PWM. In the case of a loss minimization, two cases are observed in [7], which correspond to the continuous and to the discontinuous modulation as can be seen by comparing the dependencies of the normalized harmonic power losses on the converters modulation index.

2.1.1 Modulation Techniques

Most common modulation techniques of the three-phase inverter are the carrier-based PWM (CB-PWM) and space vector PWM (SV-PWM).

**Fig. 2.1** RLE circuit of three-phase inverter
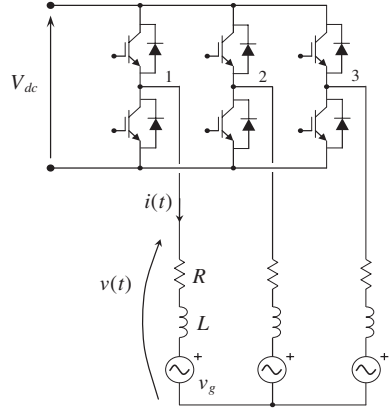
The traditional method for generating the switching patterns in three-phase VSI with CB-PWM is the use of naturally or regularly sampled sinusoidal waveforms. In general, carrier-based modulation compares a sine wave reference v^* with a triangular wave carrier signal. In naturally sampled technique the reference sine wave is allowed to vary during the carrier interval, while in regularly sampled the reference sine wave is held at a constant value during the carrier interval. Regularly sampled modulation can be symmetric, where the reference sine wave is kept constant for the whole carrier period, or asymmetric, where it is resampled in the half of the carrier period. As a result of this comparison the desired inverter switching pattern is realized. In particular, in CB-PWM schemes the three reference phase voltages v_a^*, v_b^* and v_c^* (modulating signals corresponding to the reference voltage vector in SVM), are compared with triangle carrier waveforms as represented in Fig. 2.2, for modulation index $m = 0.5$. The frequency of these carriers defines the switching frequency, and their amplitude is the half of the dc-link voltage, eventually in per units. The range of the modulation index defined as $m = V^*/V_{dc}$, in this case is $0 < m < 0.5$.

The zero-sequence injection methods, when the zero-sequence signal is added to the sine wave references, leads to a larger variety of modulating waves. The first studied technique in the literature was the third harmonic injection technique, when the 17 % third harmonic component is added to the reference waveforms. Nowadays, most used technique is the so called centered PWM, obtained by centering the reference voltages with min/max injection. Common mode signal to be added to the reference voltages (min/max injection) is defined for each phase as

$$v_{cm} = -\frac{1}{2}\left[\max\left(v_k^*\right) - \min\left(v_k^*\right)\right], \quad k = \text{a}, \text{b}, \text{c}. \tag{2.1}$$
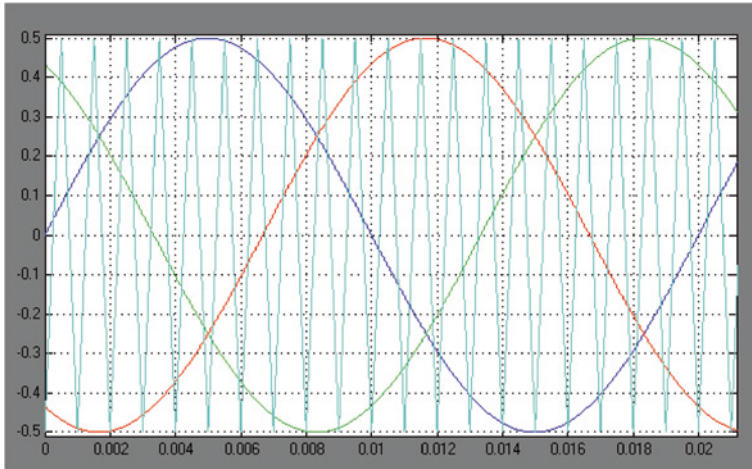
**Fig. 2.2** Carrier-based modulation, $m = 0.5$
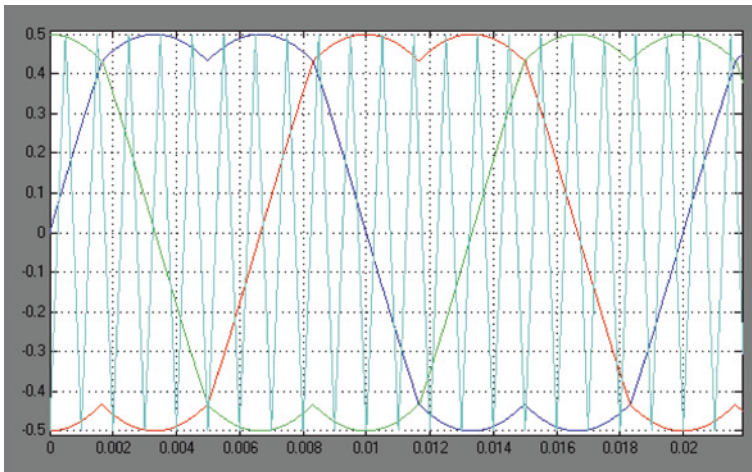
Fig. 2.3 Carrier based modulation with centered reference voltages, $m = 0.577 = m_{\text{max}}$

The resulting waveform obtained by adding the common-mode signal to the sine wave references is

$$\tilde{v}_k^* = v_k^* + v_{cm}. \tag{2.2}$$

and shown in Fig. 2.3, for modulation index $m = 0.577 = m_{\text{max}}$. Centered carrier-based modulation allows overmodulation with the respect to the original sine wave PWM, while proved that obtains better outputs spectrum and that is the optimal technique for the output ripple RMS minimization. The modulation limit is

Fig. 2.4 Space vector
diagram of inverter output
voltage
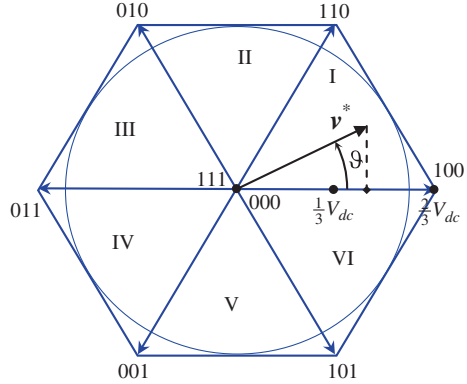
$0 < m \leq m_{\max} = 1/\sqrt{3}$, according to the generalized expression given in [8] for n phases, $m_{\max} = [2\cos(\pi/2n)]^{-1}$.

The SV-PWM of three-phase inverters is based on the determination of application times of active and null inverter voltage vectors $\mathbf{v}$ in every switching period T_s. In case of symmetrical SV-PWM, the sequence is determined in $T_s/2$ and symmetrically repeated in the next half switching period. The principle of SV-PWM in three-phase inverters is summarized with the help of Fig. 2.4, representing the output voltage space vectors corresponding to all possible switch configurations.

The output voltage space vector diagram appears to be a hexagon, consisting of 6 main triangles, numbered I–VI in Fig. 2.4. In two-level inverters the redundancy implies availability of multiple switching states to produce a given voltage vector. There is the only redundancy in zero vector with two possible states, {000} and {111}. The three nearest voltage vectors (NTV) are used to synthesize the reference output voltage space vector $\mathbf{v}^*$ in each switching period T_s, being $\mathbf{v}^* = V^* \exp(j\vartheta)$, $V^* = m\,V_{dc}$, $\vartheta = \omega t$, m the modulation index, and V_{dc} the dc-bus voltage. The switching sequence begins and ends with the null switching state.

It has been proved that the CB-PWM and SVPWM can be equivalent. By equally sharing the application time of the null voltage vector between the switch configurations 000 and 111, the centered switching pattern is realized, equivalent to the common-mode injection defined by (2.1) in carrier-based modulation, and nearly-optimal modulation able to minimize the RMS of current ripple is obtained [9].

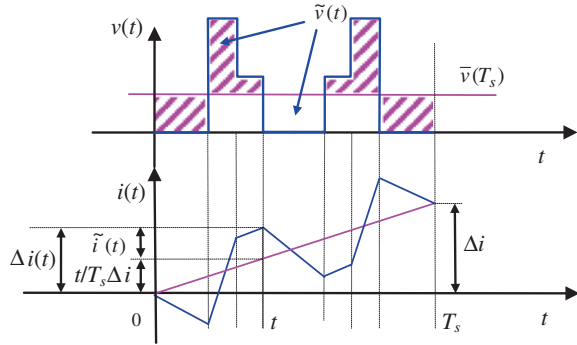## 2.2 Output Current Ripple Definition in PWM Converters

Basic circuit scheme for each phase of a balanced R–L–EMF load (RLE) is represented in Fig. 2.5. The voltage equation can be written for each phase as

$$v(t) = R\,i(t) + L\frac{di}{dt} + v_g(t). \tag{2.3}$$

Fig. 2.5 Basic RLE circuit
model for one phase
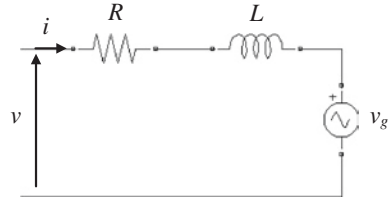
Fig. 2.6 Details of a generic
output voltage and current
ripple in the switching period

Averaging (2.3) over the switching period T_s leads to

$$\bar{v}(T_s) = R\,\bar{i}(T_s) + L\frac{\Delta i}{T_s} + \bar{v}_g(T_s), \tag{2.4}$$

being:

$$\Delta i = i(T_s) - i(0). \tag{2.5}$$

The alternating voltage $\tilde{v}(t)$ is defined as the difference between instantaneous
and average voltage components as

$$\tilde{v}(t) = v(t) - \bar{v}(T_s). \tag{2.6}$$

By introducing (2.3) and (2.4) in (2.6) leads to

$$\tilde{v}(t) = R\big[i(t) - \bar{i}(T_s)\big] + L\left[\frac{di}{dt} - \frac{\Delta i}{T_s}\right] + \big[v_g(t) - \bar{v}_g(T_s)\big]. \tag{2.7}$$

The alternating voltage component has amplitude in the order of V_{dc}, as shown
in Fig. 2.6. The first term on the right side in (2.7) accounts for the resistive voltage
drop of the current ripple, which is much lower than the rated current. The third
(last) term in (2.7) is the deviation of the generator's actual voltage from its aver-
age value in the switching period, that is negligible if $v_g(t)$ is almost sinusoidal. For
these reasons, the expression of alternating voltage component can be simplified to

$$\tilde{v}(t) \cong L\left[\frac{di}{dt} - \frac{\Delta i}{T_s}\right]. \tag{2.8}$$

The current variation in sub-period [0–t], also depicted in Fig. 2.6, can be calculated from (2.8) by integrating as

$$\Delta i(t) \cong \frac{1}{L} \int_0^t \tilde{v}(t) dt + \frac{t}{T_s} \Delta i. \tag{2.9}$$

Finally, the instantaneous current ripple $\tilde{i}(t)$ can be defined on the basis of (2.9), according to Fig. 2.6

$$\tilde{i}(t) = \Delta i(t) - \frac{t}{T_s} \Delta i \cong \frac{1}{L} \int_0^t \tilde{v}(t) dt. \tag{2.10}$$

An example of the behavior of voltage and current in a switching period is given in Fig. 2.6. Note that the current ripple (2.10) corresponds to the difference between the instantaneous current value and its fundamental component.

The peak-to-peak current ripple amplitude is defined as the range of (2.10) in the switching period

$$\tilde{i}_{pp} = \max\left\{\tilde{i}(t)\right\}_0^{T_s} - \min\left\{\tilde{i}(t)\right\}_0^{T_s}. \tag{2.11}$$

2.3 Peak-to-Peak Output Current Ripple

2.3.1 State of the Art

In the literature current ripple is studied in the terms of the RMS minimization, rather than the peak-to-peak value. An analytical approach for the analysis of current ripple in SV-PWM controlled induction motor drives for three-phase systems has been presented in [9], where the optimal SVM technique is proposed with calculation of the duty-cycles of the two zero voltage vectors, and on the basis of that the switching pattern of the optimal SVM technique is obtained. Another analysis of current ripple in a sub-period is given in [10, 11], as the error volt-second quantities which are the errors between instantaneous applied and reference voltage vectors. Of interest was to study the current ripple RMS over a sub-period and to utilize this knowledge to design hybrid PWM techniques, which reduces the line current distortion. Current ripple RMS is also analyzed in [12], for three-phase inverted feeding passive load. The analysis are conducted on one switching period and of interest was to derive RMS value of output current ripple as function of modulation index.

Newer studies on output current ripple RMS in multiphase drives are presented in [13] and [14], where a five-phase system is considered. Due to existence of more planes (two 2-D planes for five-phase systems), the concept of harmonic flux is used to mitigate initially the dependencies on the equivalent inductances in each plane, where current ripple occurs. It is shown that output current ripple RMS

cannot be minimized by injection of fifth harmonic and its odd multiples, but it is also pointed out that, from the practical point of view, differences in current ripple RMS are relatively small considering sinusoidal PWM and SV-PWM. In [14] two SV-PWM techniques are compared (four large vs. two large and two middle vectors) in terms of THD of the current and voltage with established correlations between the flux HDF and the current THD, and squared RMS current ripple. In [15] an attempt to evaluate the output RMS current ripple of a five-phase inverter has been reported, on the basis of polygon load connection and phase variables in the original domain, without the need to use space-vector theory. However, only a single (adjacent) polygon connection has been considered, and the output current-ripple RMS does not represent the total output current ripple [16].

The importance of current ripple amplitude (peak-to-peak) in three-phase systems is recognized in [17], where ripple is analyzed by introducing Thévenin equivalent circuit of the 8 different voltage vectors. In general, the evaluation of current ripple allows adjusting the switching frequency for certain ripple requirements [18]. As another example of application, the knowledge of the peak-to-peak current ripple distribution can be useful to determine the output voltage distortion due to the inverter dead-time in case of output currents with high ripple, by determining the multiple zero-crossing interval [19]. This aspect will be examined in more details in further chapter which deals with applications. Furthermore, the peak-to-peak current ripple amplitude, in addition to the fundamental current component, is useful to determine the absolute current peak, affecting the thresholds of protection systems and the design of power components

2.3.2 Calculation of the Peak-to-Peak Output Current Ripple

The output current ripple affects the noise and loss in both the PWM converter and the load, and it should be minimized to improve the system efficiency. In general, the impact of PWM techniques on the current ripple should be understood to further develop the modulation strategy. The analysis of three-phase inverters by the space vector transformation leads to better understanding and more simple calculation of voltage levels and corresponding application times. In the following analysis is considered the centered PWM, as described in Sect. 2.1.1. The reference is made to a generic balanced RLE load, representing both grid-connected and motor loads.

As result of the SV-PWM, for each phase, the average of the inverter output voltage $\bar{v}(T_s)$ corresponds to the reference voltage v^*. In the case of sinusoidal balanced output voltages supplying a balanced load, the reference output voltage vector is $v^* = m \, V_{dc} \exp(j\vartheta)$. Reference is made to Fig. 2.7. In this case, SV modulation is quarter-wave symmetric, so it can be analyzed in the range [0, 90°] of the phase angle $\vartheta = \omega t$. In particular, the two ranges $0 \leq \vartheta \leq 60°$, and $60° \leq \vartheta \leq 90°$ can be considered, as depicted in Fig. 2.7.

Fig. 2.7 Space vector diagram of inverter output voltage with six sectors and the *three identified triangles*. *Dashed circles* represent $m = 1/6, 1/3, 1/2$
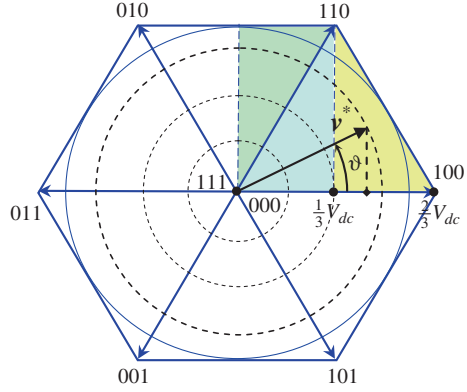
In the range $0 \leq \vartheta \leq 60°$, the application times are:

$$t_1 = m\sqrt{3}\frac{T_s}{2} \sin\left(60° - \vartheta\right), \ \{100\}, \tag{2.12}$$

$$t_2 = m\sqrt{3}\frac{T_s}{2} \sin \vartheta, \ \{110\}, \tag{2.13}$$

$$t_0 = \frac{T_s}{2} - (t_1 + t_2) = \frac{T_s}{2}\left[1 - \sqrt{3}m \sin\left(60° + \vartheta\right)\right], \ \begin{Bmatrix} 000 \\ 111 \end{Bmatrix}. \tag{2.14}$$

In the range $60° \leq \vartheta \leq 90°$, the application times are:

$$t_1 = m\sqrt{3}\frac{T_s}{2} \sin\left(120° - \vartheta\right), \ \{110\}, \tag{2.15}$$

$$t_2 = m\sqrt{3}\frac{T_s}{2} \sin\left(\vartheta - 60°\right), \ \{010\}, \tag{2.16}$$

$$t_0 = \frac{T_s}{2} - (t_1 + t_2) = \frac{T_s}{2}\left[1 - \sqrt{3}m \sin \vartheta\right], \ \begin{Bmatrix} 000 \\ 111 \end{Bmatrix}. \tag{2.17}$$

Due to the symmetry among the three phases in the considered case of sinusoidal balanced currents, only the first phase is examined in the following analysis. In terms of space vectors, the variables of the first phase are given by the projection of the corresponding space vectors on the real axes. In particular, the average output voltage is given by

$$\bar{v}(T_s) = v^* = \text{Re}\{v^*\} = V^* \cos \vartheta = V_{dc}m \cos \vartheta. \tag{2.18}$$

By introducing (2.18) in (2.6), the alternative component of inverter output voltage of the first phase can be written as

Fig. 2.8 Output voltage
and current ripple in
one switching period
$(0 \le \vartheta \le 60°, 0 \le m$
$\cos \vartheta \le 1/3)$
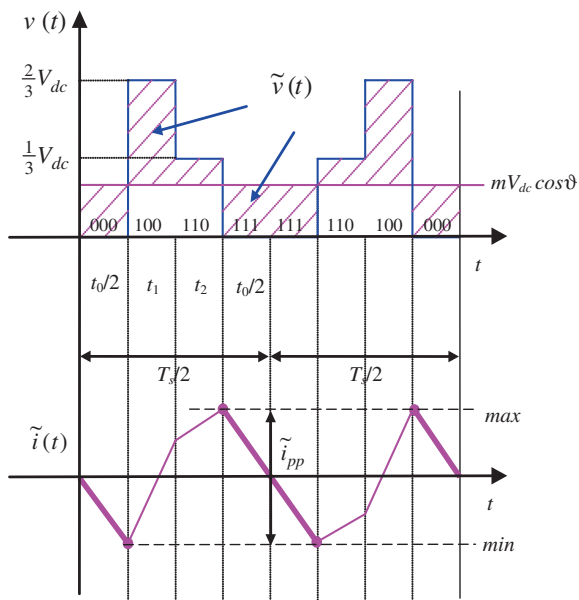
$$\tilde{v}(t) = \left[S_1 - \frac{1}{3}(S_1 + S_2 + S_3) \right] V_{dc} - mV_{dc} \cos \vartheta, \tag{2.19}$$

being $S_k = [0, 1]$ the switch state of the k-th inverter leg. In order to evaluate the
current ripple in the whole phase angle range $0 < \vartheta < 90°$, the three different trian-
gles depicted in Fig. 2.7 must be separately considered.

1. *Evaluation in the range* $0 \le \vartheta \le 60°$

Considering the first sector of the hexagon, $0 \le \vartheta \le 60°$, two different cases can
be distinguished, $0 \le m \cos \vartheta \le 1/3$ and $m \cos \vartheta \ge 1/3$, corresponding to the two
colored triangular regions in Fig. 2.7.

For modulation index $0 \le m \cos \vartheta \le 1/3$, the current ripple $\tilde{i}$ and its peak-to-
peak value $\tilde{i}_{pp}$ are depicted in Fig. 2.8, together with the instantaneous output volt-
age $v(t)$. According to Fig. 2.8, $\tilde{i}_{pp}$ can be evaluated by (2.10), (2.11), and (2.19),
considering application interval t_0 (light blue area in Fig. 2.7), leading to

$$\tilde{i}_{pp} = \frac{1}{L} \{ V_{dc} m \cos \vartheta \, t_0 \}. \tag{2.20}$$

The case of $1/3 \le m \cos \vartheta \le 1/\sqrt{3}$ is depicted in Fig. 2.9. In this case $\tilde{i}_{pp}$ can be
evaluated considering the application intervals $t_0/2$ and t_2 (yellow area in Fig. 2.7),
leading to

$$\tilde{i}_{pp} = \frac{2}{L} \left\{ V_{dc} m \cos \vartheta \frac{t_0}{2} + \left(V_{dc} m \cos \vartheta - \frac{V_{dc}}{3} \right) t_2 \right\}. \tag{2.21}$$

Fig. 2.9 Output voltage and current ripple in one switching period $(0 \leq \vartheta \leq 60°, m \cos \vartheta > 1/3)$
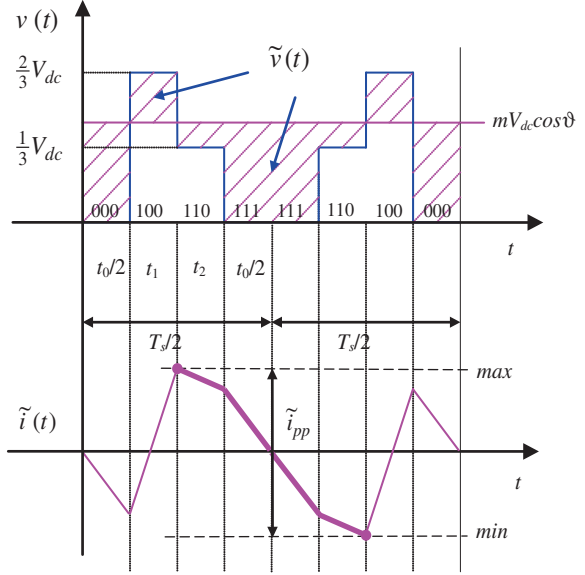
For both cases (2.20) and (2.21), introducing the expressions for application intervals $t_0/2$ and t_2, (2.14) and (2.13), peak-to-peak current ripple can be written as

$$\tilde{i}_{pp} = \frac{V_{dc}T_s}{2L}r(m, \vartheta),\tag{2.22}$$

being $r(m, \vartheta)$ the normalized peak-to-peak current ripple amplitude given by

$$r(m, \vartheta) = m \cos \vartheta \left[1 - \sqrt{3}m \sin \left(\vartheta + 60°\right)\right], \quad 0 \leq m \cos \vartheta \leq \frac{1}{3}, \tag{2.23}$$

$$r(m, \vartheta) = m \left\{ \cos \vartheta \left[1 - \sqrt{3}m \sin \left(\vartheta + 60°\right)\right] \right.$$
$$\left. + 2\sqrt{3} \sin \vartheta \left(m \cos \vartheta - \frac{1}{3}\right) \right\}, \quad \frac{1}{3} \leq m \cos \vartheta \leq \frac{1}{\sqrt{3}}. \tag{2.24}$$

2. *Evaluation in the range* $60° \leq \vartheta \leq 90°$

Considering the third triangle depicted in Fig. 2.7, (green area), $60° \leq \vartheta \leq 90°$, the peak-to-peak current ripple amplitude can be determined considering the application intervals $t_0/2$ and t_2 for all modulation indexes, according to Fig. 2.10. Introducing (2.19) in (2.10) and (2.11) leads to
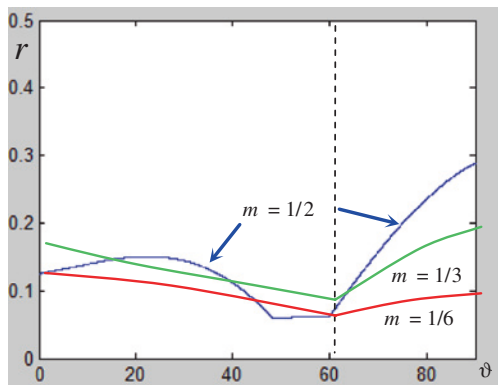
$$\tilde{i}_{pp} = \frac{2}{L}\left\{V_{dc}m \cos \vartheta \frac{t_0}{2} + \left[V_{dc}m \cos \vartheta + \frac{1}{3}V_{dc}\right]t_2\right\}.\tag{2.25}$$

Considering the expressions for application intervals t_0 and t_2, (2.17) and (2.16), normalized current ripple amplitude is

Fig. 2.10 Output voltage and current ripple in one switching period ($60° \leq \vartheta \leq 90°$)
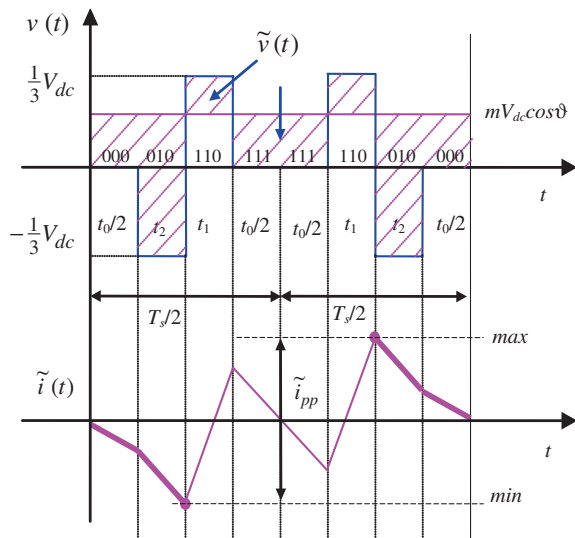
Fig. 2.11 Normalized peak-to-peak current ripple amplitude $r(m, \vartheta)$ for three modulation indexes, $m = 1/6$, $1/3$, and $1/2$, in the phase angle range $[0, 90°]$

$$r(m, \vartheta) = m \left\{ \frac{1}{\sqrt{3}} \sin \vartheta - 3m \cos^2 \vartheta \right\}. \tag{2.26}$$

2.3.3 Peak-to-Peak Current Ripple Diagrams

In order to show the behavior of the peak-to-peak current ripple amplitude in the fundamental period for all the possible cases, in Figs. 2.11 and 2.12 is represented the normalized function $r(m, \vartheta)$ defined by (2.22). Figure 2.11 shows $r(\vartheta)$ for $m = 1/6$, $1/3$, and $1/2$, corresponding to the dashed circles in Fig. 2.7. Since symmetric PWM modulation is considered, ripple is symmetric as well, so the ripple envelope corresponds to the half of $\tilde{i}_{pp}$. The two regions ($0 \leq \vartheta \leq 60°$ and

Fig. 2.12 Map of the
normalized peak-to-peak
current ripple amplitude
$r(m, \vartheta)$
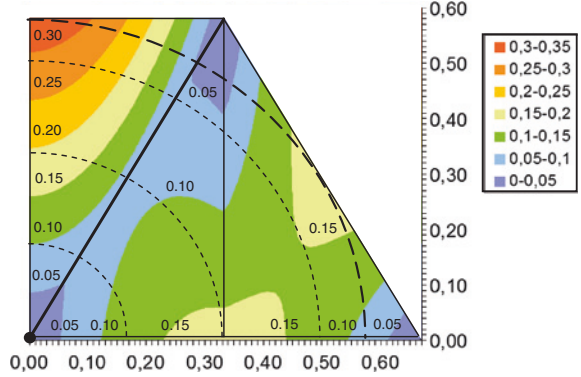
$60° \leq \vartheta \leq 90°$) can be distinguished for $m = 1/6$ and $1/3$. All the three regions are visible for $m = 1/2$, according to Fig. 2.7.

Figure 2.12 shows the colored map of $r(m, \vartheta)$ in the 1st quadrant within the modulation limits. The ripple amplitude is almost proportional to m in the neighborhoods of $m = 0$. Phase angle with minimum ripple can be identified, that is $\vartheta \approx 50° \div 60°$, and a phase angle with maximum ripple, that is $\vartheta = 90°$. These aspects are further developed in the following section.

2.3.4 Maximum and Minimum of the Current Ripple

In order to estimate current ripple amplitude in the whole fundamental period, the maximum and the minimum of the current ripple can be evaluated. For this purpose, four relevant points can be noticed in Figs. 2.11 and 2.12, as mentioned above: two local maxima, for $\vartheta = 0$ and for $\vartheta = 90°$, and two local minima for $\vartheta = 60°$ and for $m \cos \vartheta = 1/3$, i.e., around $\vartheta = 50°$.

To determine the local maxima, $\vartheta = 0$ can be set in (2.23), and $\vartheta = 90°$ in (2.26), leading to the following global maximum

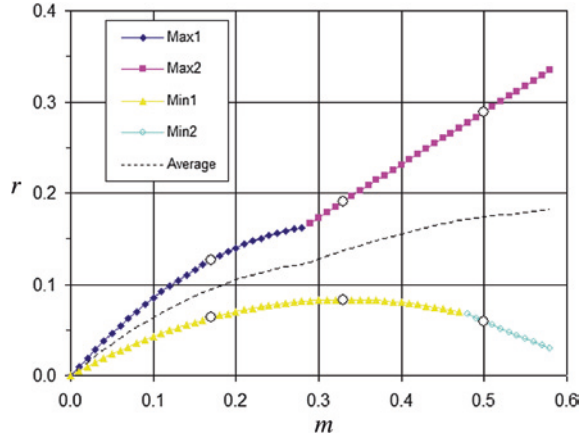$$r^{\max}(m) = \max\left\{ m\left[1 - \frac{3}{2}m\right], \frac{1}{\sqrt{3}}m \right\}. \tag{2.27}$$

The intersection between the two local maxima gives the border value of modulation index

$$m\left[1 - \frac{3}{2}m\right] = \frac{1}{\sqrt{3}}m, \tag{2.28}$$

leading to $m \approx 0.282$. Finally, combining (2.27) and (2.28), the maximum of normalized current ripple is

$$r^{\max}(m) = \begin{cases} m\left[1 - \frac{3}{2}m\right] & \text{for} \quad m < 0.282, \\ \frac{1}{\sqrt{3}}m & \text{for} \quad m > 0.282. \end{cases} \tag{2.29}$$

Fig. 2.13 Maximum and
minimum of normalized
peak-to-peak current ripple
amplitude as function of
modulation index

In order to determine the local minima, $\vartheta = 60°$ can be set in either (2.23) or
(2.26), and $m \cos \vartheta = 1/3$ in (2.23). The expression for the global minimum of
normalized current ripple is

$$r^{\min}(m) = \min\left\{ m\left[\frac{1}{2} - \frac{3}{4}m\right], \frac{1}{6}\left[1 - \sqrt{3m^2 - \frac{1}{3}}\right] \right\}. \qquad (2.30)$$

The intersection between the two local minima gives the border value of the
modulation index

$$m\left[\frac{1}{2} - \frac{3}{4}m\right] = \frac{1}{6}\left[1 - \sqrt{3m^2 - \frac{1}{3}}\right], \qquad (2.31)$$

leading to $m \approx 0.479$. Finally, combining (2.30) and (2.31), the minimum of
normalized current ripple is

$$r^{\min}(m) = \begin{cases} m\left[\frac{1}{2} - \frac{3}{4}m\right] & \text{for} \quad m < 0.479, \\ \frac{1}{6}\left[1 - \sqrt{3m^2 - \frac{1}{3}}\right] & \text{for} \quad m > 0.479. \end{cases} \qquad (2.32)$$

The composition of the two local minima and maxima are given in Fig. 2.13,
leading to global maximum and minimum. The approximated average value is pre-
sented with dashed line. The white dots represent the specific points for $m = 1/6$,
1/3, and 1/2, displayed in Fig. 2.11, and further examined in simulations and experi-
ments. It can be noted that the maximum function is almost linear for every modula-
tion index, strictly for $m > 0.282$. Then, on the basis of (2.22) and (2.29), a simplified
expression for maximum of peak-to-peak current ripple amplitude is obtained as

$$\tilde{i}_{pp}^{\max} \cong \frac{V_{dc}T_s}{2\sqrt{3}L}m. \qquad (2.33)$$

Fig. 2.14 The average of
the normalized peak-to-peak
current ripple amplitude as
function of modulation index
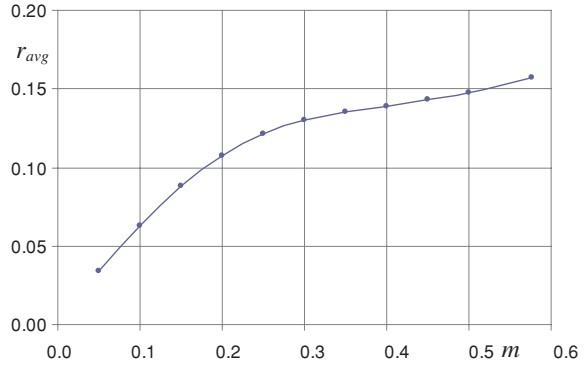
The exact average of the normalized peak-to-peak current ripple, calculated for
the more points, is presented in Fig. 2.14. It shows very similar behavior to the
approximated one shown in Fig. 2.13. Almost linear behavior can be observed for
the modulation indexes $m > 0.282$.

2.4 Numerical and Experimental Results

In order to verify the analytical developments proposed in previous sections, numeri-
cal simulations and corresponding experimental tests are carried out. Circuit simula-
tions are performed by Sim-PowerSystems of Matlab considering three-phase inverter
with ideal switches connected to sinusoidal voltage sources by RL impedance, having
$R = 4\ \Omega$ and $L = 24$ mH. Power transistors have been modeled with ideal switches in
order to have a very precise matching with the analytical developments. By introduc-
ing non idealities in simulations, such as commutation times, voltage drops, parasitic
elements, dead-times etc., leads to output voltage distortion with additional harmonics
[20], making more difficult the validation of the proposed theoretical approach. This
topology could represent a general three-phase inverter with either motor or grid-con-
nected loads. In all simulations the fundamental frequency is set to 50 Hz, the switching
frequency $1/T_s$ is 2.1 kHz, and the dc voltage supply V_{dc} is 600 V. A centered symmetri-
cal carrier-based PWM technique, equivalent to centered space vector modulation, is
considered in both simulations and experiments, being easier for the implementation.

The experimental setup with custom-built two-level three-phase inverter is
shown in Fig. 2.15. Power switches are Infineon FS50R12KE3 IGBT pack.
DSpace ds1006 hardware has been employed for the real-time implementation of
the algorithm. Dc-bus voltage (V_{dc}) is set to 600 V by Sorensen SGI 600/25 dc
supply. Switching frequency was set to 2.1 kHz and the inverter's dead time of
6 μs (not compensated) is implemented in the hardware. Fundamental frequency
was kept at 50 Hz for easier comparison with analytical developments. The nearly-
optimal centered space vector PWM is implemented.

The load was a three-phase induction motor (mechanically unloaded). Main
motor parameters (all referred to stator) are: stator resistance $R_s = 2.4\ \Omega$, rotor
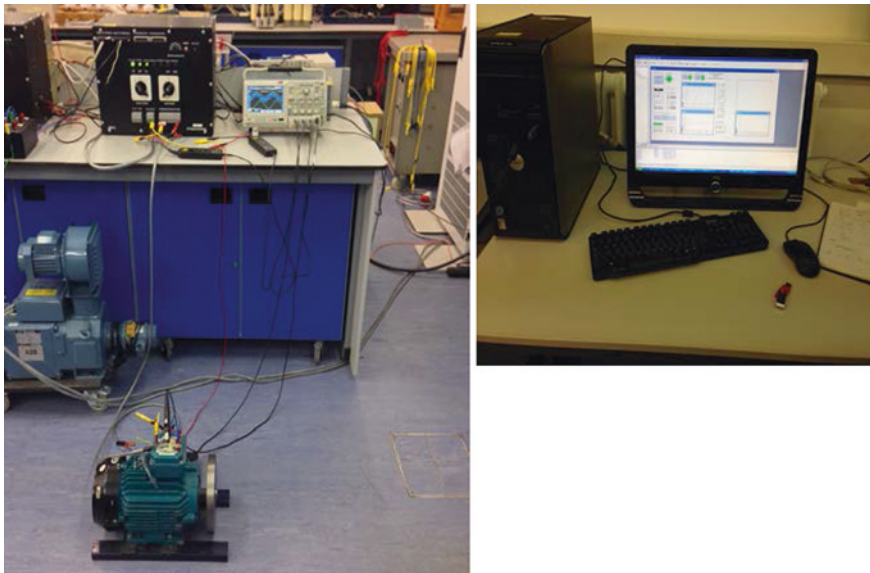
Fig. 2.15 Experimental setup

resistance $R'_r = 1.6\ \Omega$, stator leakage inductance $L_{ls} = 12$ mH, rotor leakage inductance $L'_{lr} = 12$ mH, magnetizing inductance $L_m = 300$ mH, and pole pairs $p = 2$. According to the model of induction motor for higher order harmonics, which are determining the current ripple, the equivalent inductance $L = L_{ls} + L'_{lr} = 24$ mH is considered for the ripple evaluation.

Tektronix oscilloscope MSO2014 with current probe TCP0030 was used for measurements, and the built-in noise filter (cut-off frequency $f_c = 600$ kHz) was applied. The instantaneous current ripple $\tilde{i}$ in both simulations and experiments is calculated as the difference between the instantaneous current and its fundamental component, i.e.

$$\tilde{i}(t) = i(t) - I_{fund}(t). \tag{2.34}$$

The three-phase system is well balanced and the first phase is selected for further analysis, as in analytical developments. Different values of m have been investigated ($1/6$, $1/4$, $1/3$, $1/2$, and $1/\sqrt{3} = m_{max}$).

In Figs. 2.16, 2.18, 2.20, 2.22, and 2.24 is shown the current ripple obtained with simulations (a) and experiments (b), for different modulation indexes, respectively. Comparison is made with the half of the peak-to-peak current ripple, $\tilde{i}_{pp}/2$. Positive and negative envelopes (blue traces) are determined by the equations presented in Sect. 2.3.2. The corresponding experimental results are shown as gray traces.

In Figs. 2.17, 2.19, 2.21, 2.23, and 2.25 is depicted the instantaneous output current obtained in simulations (a) and experiments (b) with different modulation indexes, respectively. Current is shown with the calculated upper/lower ripple envelope, depicted in blue colors. The corresponding experimental results are shown in grey traces.
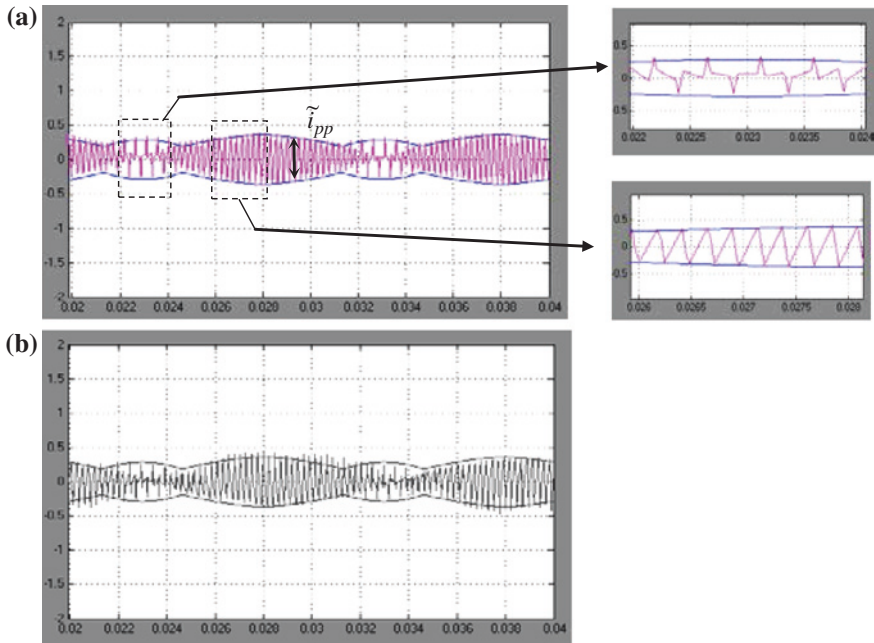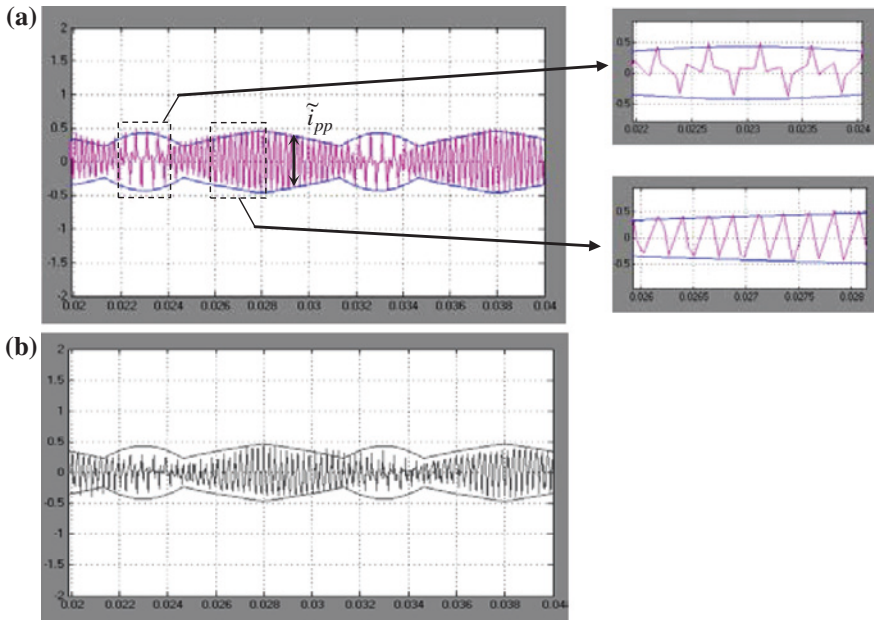
Fig. 2.16 Current ripple (*pink*), $m = 1/6$, and evaluated peak-to-peak envelope (*blue*) for one fundamental period: **a** simulation, with details, and **b** experimental results
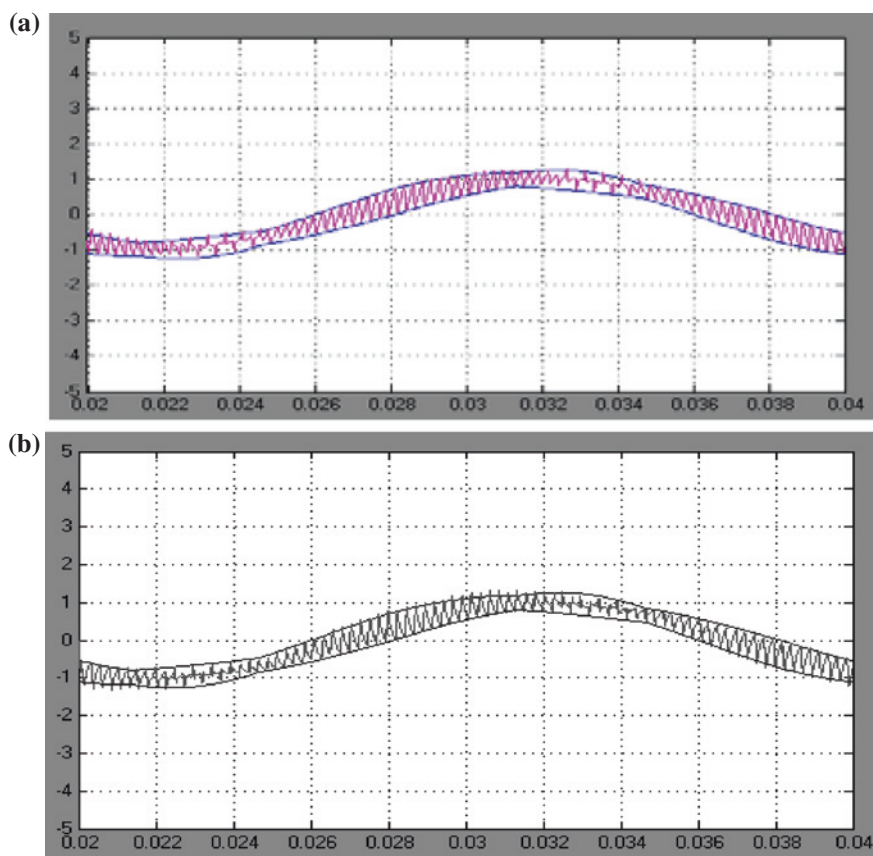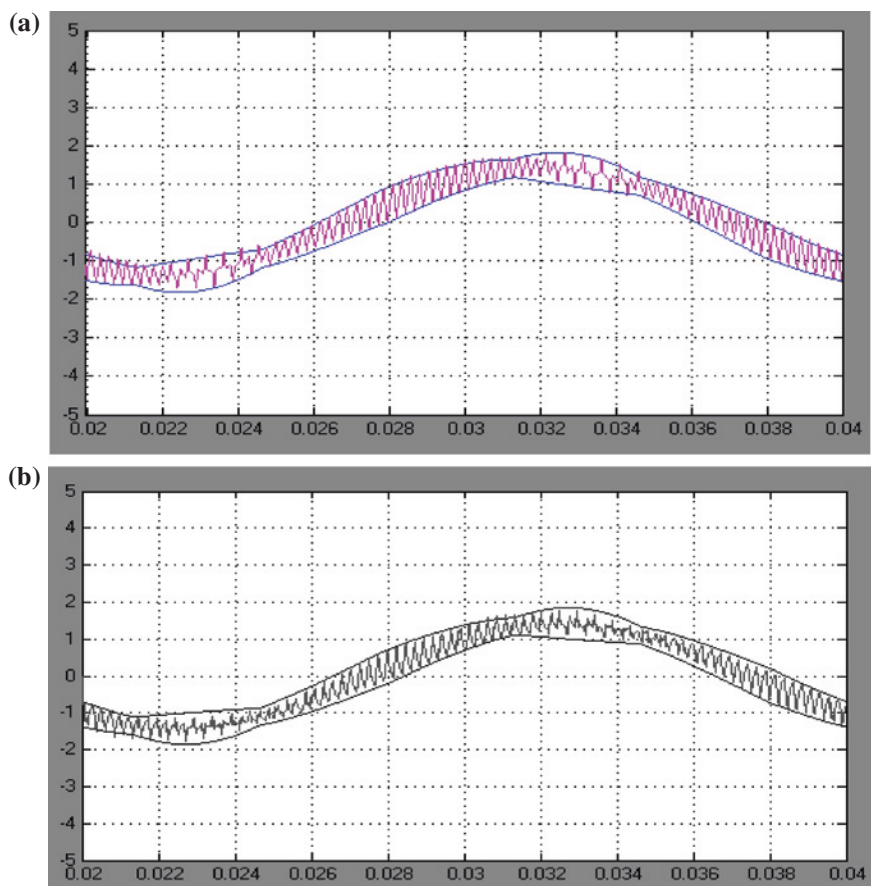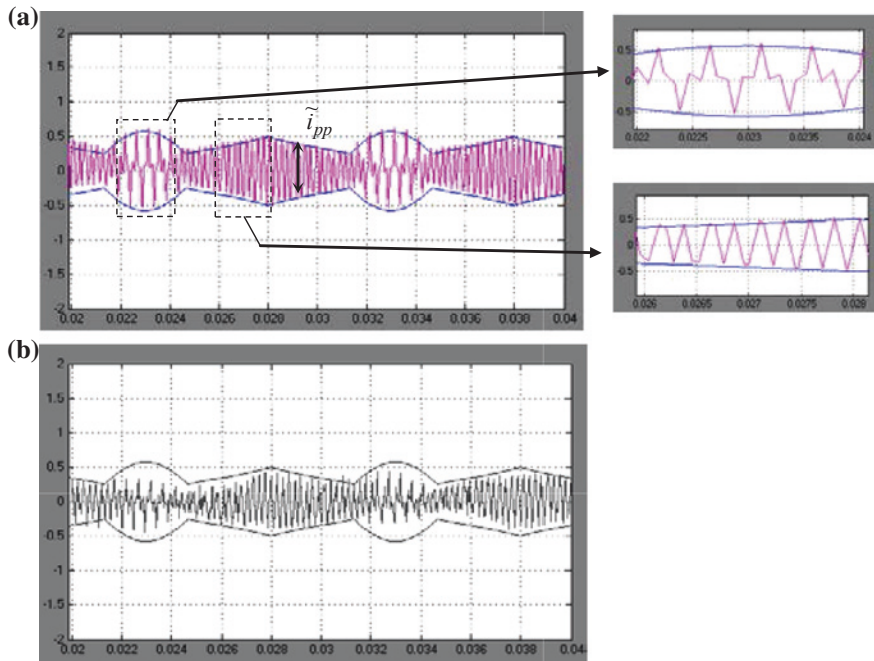
Fig. 2.17 Instantaneous output current (*pink*) with calculated current envelopes (*blue traces*) for $m = 1/6$: **a** simulated, **b** experimental results
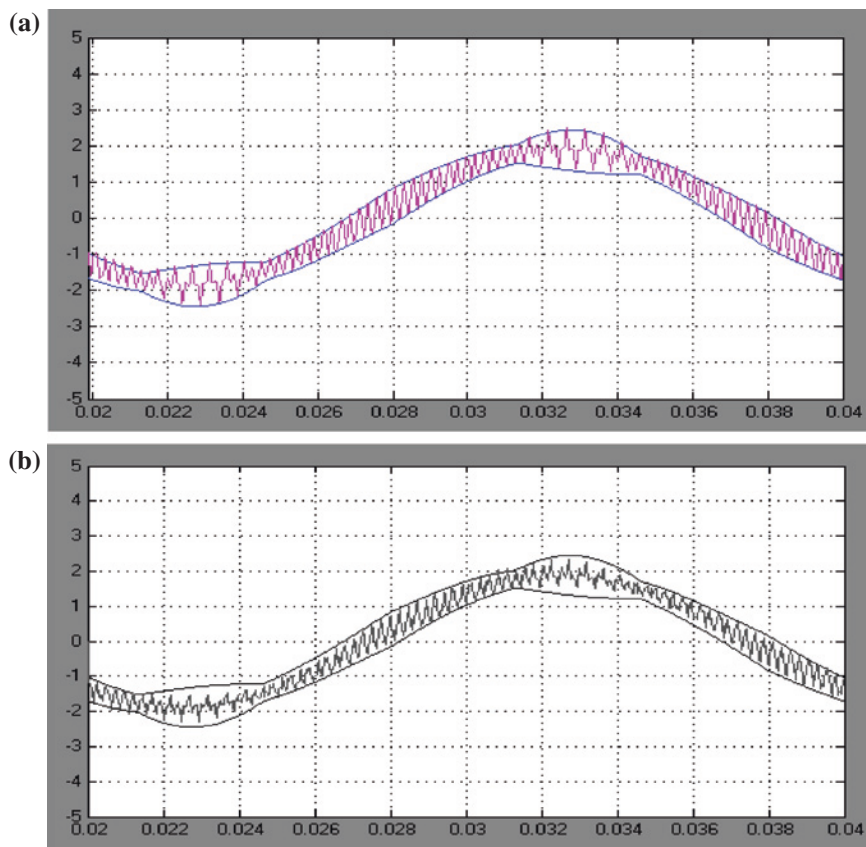
Fig. 2.18 Current ripple (*pink*), $m = 1/4$, and evaluated peak-to-peak envelope (*blue*) for one fundamental period: **a** simulation, with details, and **b** experimental results

(a)

(b)

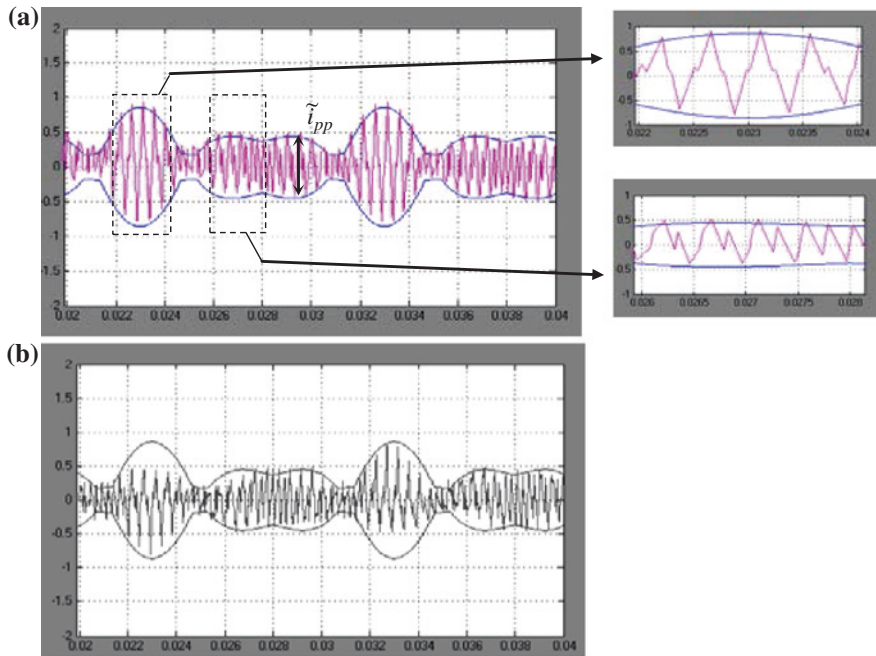
Fig. 2.19 Instantaneous output current (*pink*) with calculated current envelopes (*blue traces*) for $m = 1/4$: **a** simulated, **b** experimental results

Fig. 2.20 Current ripple (*pink*), $m = 1/3$, and evaluated peak-to-peak envelope (*blue*) for one fundamental period: **a** simulation, with details, and **b** experimental results

(a)

(b)

Fig. 2.21 Instantaneous output current (*pink*) with calculated current envelopes (*blue traces*) for $m = 1/3$: **a** simulated, **b** experimental results
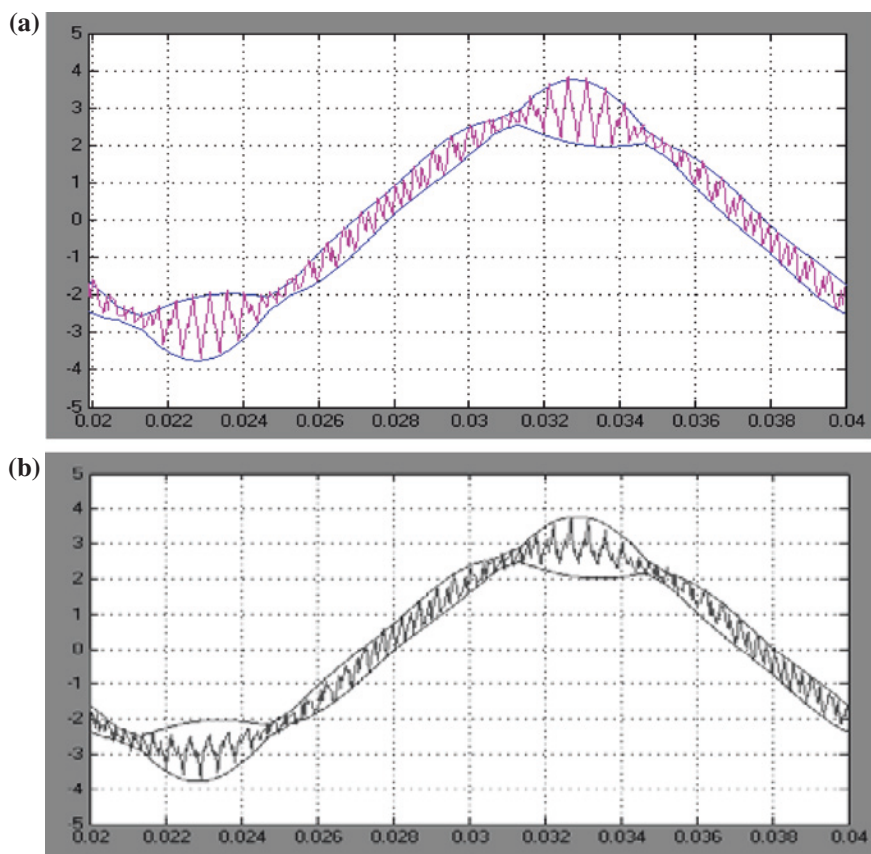
Fig. 2.22 Current ripple (*pink*), $m = 1/2$, and evaluated peak-to-peak envelope (*blue*) for one fundamental period: **a** simulation, with details, and **b** experimental results
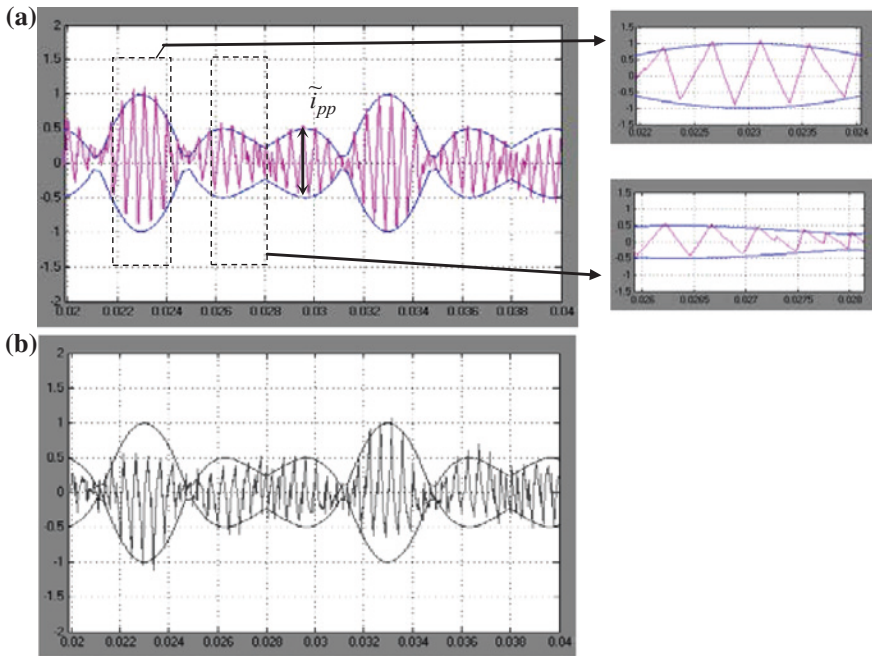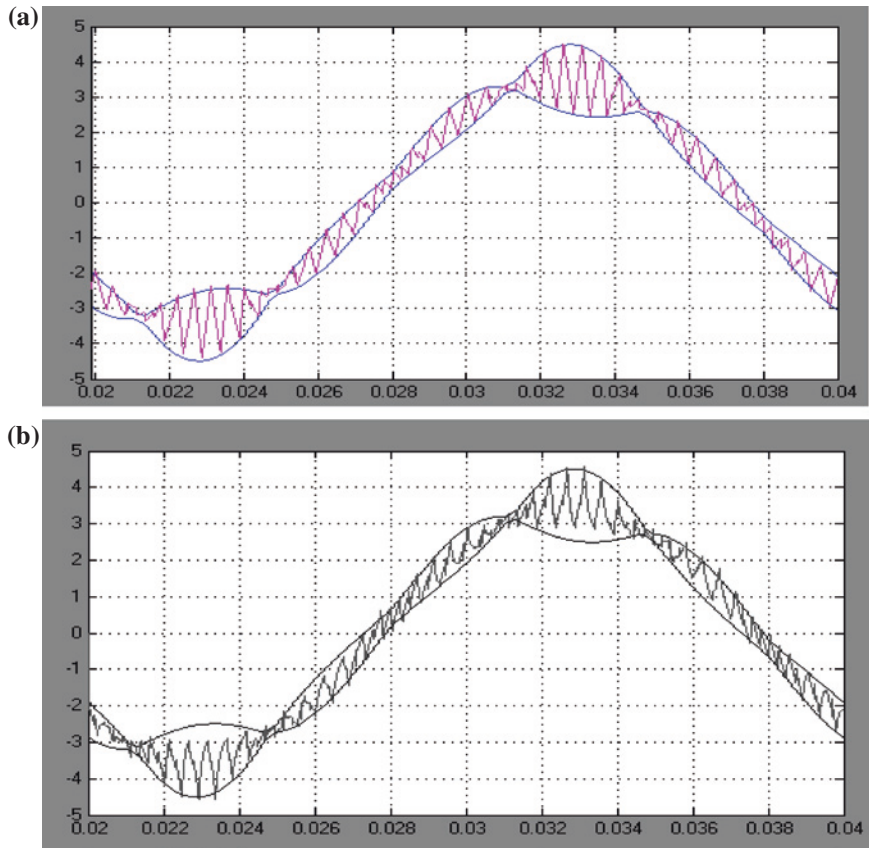
(a)

(b)

Fig. 2.23 Instantaneous output current (*pink*) with calculated current envelopes (*blue traces*) for $m = 1/2$: **a** simulated, **b** experimental results

Fig. 2.24 Current ripple (*pink*), $m = 1/\sqrt{3} = m_{max}$, and evaluated peak-to-peak envelope (*blue*) for one fundamental period: **a** simulation, with details, and **b** experimental results

Fig. 2.25 Instantaneous output current (*pink*) with calculated current envelopes (*blue traces*) for $m = 1/\sqrt{3} = m_{\text{max}}$: **a** simulated, **b** experimental results

The values of the modulation index cover all possible sub-cases (different colored regions in Fig. 2.6). The agreement is almost good in the whole fundamental period. Small mismatches can be observed in the experimental current ripple, especially for the higher modulation indexes. These mismatches were probably introduced by the dead-times which in this case were not compensated, but this point can be further examined in the future work.

References

1. A.M. Hava, R.J. Kerkman, T.A. Lipo, Carrier-based PWM-VSI overmodulation strategies: analysis, comparison, and design. IEEE Trans. Power Electron. **13**(4), 674–689 (1998)
2. D. Zhao, V.S.S. Pavan Kumar Hari, G. Narayanan, R. Ayyanar, Space-vector hybrid pulsewidth modulation techniques for reduced harmonic distortion and switching loss. IEEE Trans. Power Electron. **25**(3), 760–774 (2010)
3. D. Casadei, M. Mengoni, G. Serra, A. Tani, L. Zarri, A new carrier-based PWM strategy with minimum output current ripple for five-phase inverters, in *Proceedings of the 14th European Conference on Power Electronics and Applications (EPE)*, Birmingham UK, 30 Aug 2011–1 Sept 2011, pp. 1–10
4. X. Mao, R. Ayyanar, H.K. Krishnamurthy, Optimal variable switching frequency scheme for reducing switching loss in single-phase inverters based on time-domain ripple analysis. IEEE Trans. Power Electron. **24**(4), 991–1001 (2009)
5. G.D. Holmes, T.A. Lipo, *Pulse Width Modulation for Power Converters: Principles and Practice*. (IEEE Press Series on Power Engineering, Wiley, Piscataway, NJ, USA, 2003)
6. J.W. Kolar, H. Ertl, F.C. Zach, Influence of the modulation method on the conduction and switching losses of a PWM converter system. IEEE Trans. Ind. Appl. **27**(6), 1063–1075 (1991)
7. J.W. Kolar, H. Ertl, F.C. Zach, Minimizing the current harmonics RMS value of three-phase PWM converter systems by optimal and suboptimal transition between continuous and discontinuous modulation, in *Proceedings of 22nd Annual IEEE Power Electronics Specialists Conference (PESC '91)*, Cambridge, MA, 24–27 June 1991, pp. 372–381
8. E. Levi, D. Dujic, M. Jones, G. Grandi, Analytical determination of DC-bus utilization limits in multi-phase VSI supplied AC drives. IEEE Trans. Energy Convers. **23**(2), 433–443 (2008)
9. D. Casadei, G. Serra, A. Tani, L. Zarri, Theoretical and experimental analysis for the RMS current ripple minimization in induction motor drives controlled by SVM technique. IEEE Trans. Ind. Electron. **51**(5), 1056–1065 (2004)
10. G. Narayanan, D. Zhao, H.K. Krishnamurthy, R. Ayyanar, V.T. Ranganathan, Space vector based hybrid PWM techniques for reduced current ripple. IEEE Trans. Ind. Electron. **55**(4), 1614–1627 (2008)
11. T.B. Reddy, J. Amarnath, D. Subbarayudu, New hybrid SVPWM methods for direct torque controlled induction motor drive for reduced current ripple, in *Proceedings of International Conference on Power Electronics, Drives and Energy Systems (PEDES '06)*, New Delhi, India, 12–15 Dec 2006, pp. 1–6
12. A. Murnandityo, P.A. Dahono, Analysis of output current ripple of three-phase PWM inverter under discontinuous modulation techniques, in *Industrial Electronic Seminar* (2010)
13. D. Dujic, M. Jones, E. Levi, Analysis of output current ripple rms in multiphase drives using space vector approach. IEEE Trans. Power Electron. **24**(8), 1926–1938 (2009)
14. M. Jones, D. Dujic, E. Levi, J. Prieto, F. Barrero, Switching ripple characteristics of space vector PWM schemes for five-phase two-level voltage source inverters-Part 2: current ripple. IEEE Trans. Ind. Electron. **58**(7), 2799–2808 (2011)
15. P.A. Dahono, Deni, E.G. Supriatna, Output current-ripple analysis of five-phase PWM inverters. IEEE Trans. Ind. Appl. **45**(6), 2022–2029 (2009)
16. D. Dujic, M. Jones, E. Levi, Analysis of output current-ripple RMS in multiphase drives using polygon approach. IEEE Trans. Power Electron. **25**(7), 1838–1849 (2010)
17. D. Jiang, F. Wang, Current-ripple prediction for three-phase PWM converters. IEEE Trans. Ind. Appl. **50**(1), 531–538 (2014)
18. D. Jiang, F. Wang, Variable switching frequency PWM for three-phase converters based on current ripple prediction. IEEE Trans. Power Electron. **28**(11), 4951–4961 (2013)
19. G. Grandi, J. Loncarski, R. Seebacher, Effects of current ripple on dead-time analysis of three-phase inverters, in *Proceedings of IEEE Energy Conference (ENERGYCON)*, Florence, Italy, 9–12 Sept 2012, pp. 207–212

20. G. Grandi, J. Loncarski, Analysis of dead-time effects in multi-phase voltage source inverters, in *Proceedings of IET Power Electronics, Machines and Drives (PEMD)*, Bristol, UK, 27–29 Mar 2012, CD-ROM paper 0223

Authored Papers

G. Grandi, J. Loncarski, Evaluation of current ripple amplitude in three-phase PWM voltage source inverters, in *Proceedings of 8th IEEE International Conference on Compatibility and Power Electronics, CPE*, Ljubljana, Slovenia, 5–7 June 2013. doi:10.1109/CPE.2013.6601146

Peak-to-Peak Output Current Ripple Analysis in
Multiphase and Multilevel Inverters
Loncarski, J.